Journal of Engineering Mathematics **38:** 51–76, 2000.

An asymptotic approach to the mathematical modeling of Ohno continuous casting of cored rods

S. A. MORMAN and G. W. YOUNG
Department of Mathematical Sciences, The University of Akron, Akron, Ohio 44325-4002, U.S.A.

Received 30 December 1997; accepted in revised form 15 June 1999

Abstract. A model is presented to simulate Ohno Continuous Casting (OCC) of cored rods. Equations describing the axisymmetric transport of heat in the mold and cored rod are discussed. Heat transfer between the system and the surrounding environment is assumed to take place via convection. If the velocity of casting, the external temperature profile, the mold temperature, and the mold-cooler distance are given, asymptotic solutions for the temperature profile in the rod are found and expressions for the solidifying interfacial shapes are developed in the limit of a small melt slenderness ratio (mold radius/mold length). The effect of process parameters on the shape of the cored rod system is investigated.

Key words: asymptotic expansions, Ohno casting, heat transfer, metal casting, solidification.

1. Introduction

The Ohno Continuous Casting process (OCC) (developed by A. Ohno at the Chiba Institute of Technology in Japan) is used to grow single crystals and to produce cored materials with unidirectional crystal structure [1–10]. This process differs from conventional continuous casting procedures in that molten metal is poured into a heated mold, rather than one that is cooled. The OCC mold has a temperature slightly higher than the solidification temperature of the metal. See Figures 1 and 2. The crystal growth may then occur near the exit of the mold. This practically eliminates friction between the mold and cast product, which often results in tearing or pitting of the cast surface. The heated mold also makes it possible to place a hollow mandrel within the mold [4, 9], through which liquid core alloys are fed to produce a core product with unidirectional columnar crystals in the longitudinal direction of the cast.

The OCC process is currently being implemented in a variety of commercial applications. For example, the OCC technique is being used to cast 8 mm diameter rods of 18 karat gold alloys that have been successfully drawn to wires of 0·25 mm in diameter, which could not otherwise be produced by conventional methods [9]. Single crystal copper wires of different diameters have been grown for use as conductors in audio and video equipment [9]. The process has also been used to produce copper tubing products with internal fins and partitions for applications such as heat-exchanger tubes and induction coils [1], and has been applied to the manufacturing of tubes containing optical fibers. Optical fiber sensors have been considered in the design and construction of modern structures such as bridges, buildings and hydroelectric dams. They can be attached to the surface of, or embedded into these materials and structures and used to continuously monitor physical conditions such as damage, strain, or temperature [10]. In these applications a metallic cladding for the fiber is needed to protect it

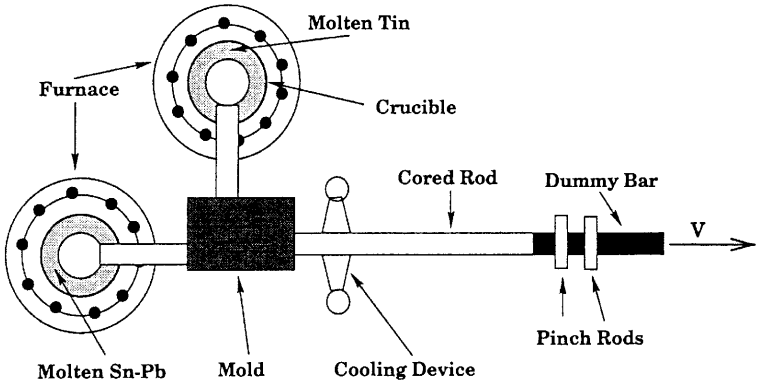

Figure 1. Schematic of casting arrangement.

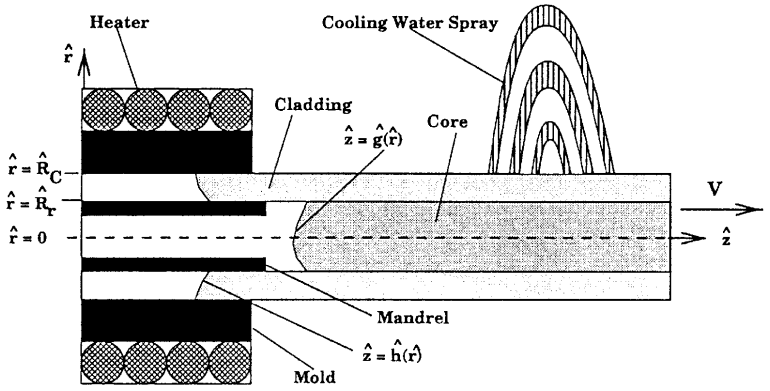

Figure 2. Double channel mold–rod system. The shaded regions denote the solid core and cladding.

from the harsh environment. The OCC technique offers an alternative to coating and chemical vapor deposition (CVD) processes to produce the outer cladding.

This study will consider casting a pure-tin-clad layer outside of a core of Sn-Pb eutectic alloy. The objective of this study is to obtain an understanding of the casting of cored materials using a heated double-channel OCC mold. A schematic of this OCC process is shown in Figure 1 [9]. The equipment consists of two crucibles for melting and containing the pure tin and the Sn-Pb alloy, level control devices, a withdrawal device for the cast rod, and a double-channel mold, which is 40 mm long, has an outer channel with a 10 mm bore which defines the rod diameter, and an inner channel 10 mm long, created by the mandrel, with 3·5 mm inner diameter and 5 mm outer diameter, which determines the core diameter of the cast product [4].

The key to this method is the use of the double channel mold, with a mandrel placed inside, as shown in Figure 2. The core alloy is fed through a hole in the mandrel, and then into the tube created by the mandrel, with the clad material passing on the outside of the mandrel. The mold permits a single casting operation to produce cored materials whose core and cladding contain unidirectional structures.

The purpose of this paper is to determine the location and shape of the solidification fronts in both the core and clad materials. Slight changes in these locations significantly affect the quality of the cast [6]. First, the location of the clad front is important because, if it is located far into the mold, the friction created with the mold can cause tearing to occur on the outside of

the cast rod. Hence, it is desirable to set the processing parameters so that this front is as close as possible to the mold exit. Then again, it cannot be too close to the exit, because mechanical vibration and hydrostatic pressure can cause the diameter of the growing rod to vary, which leads to a non-constant cross-sectional area in the final rod [4, 10]. In addition, the core must solidify to the right of the mandrel or there will be a hollow channel between the cladding and core. The remainder of this paper will consist of the development and subsequent testing of a mathematical model of this system.

There has been an extensive amount of investigation in the literature of Stefan-type problems [11–30, for example], directional solidification configurations [31–40, for example], and conventional casting [41–57, for example]. Exact solutions to these classes of problems are generally restricted to unbounded domains, and subject to limitations on the boundary conditions (for example, constant temperature). For this reason, a variety of approximate analytical and numerical approaches have been developed to examine domains and boundary conditions which more closely simulate actual processing conditions.

Analytical approaches have generally been concerned with one-dimensional, planar interface, time-dependent models, or two-dimensional, steady-state models. In the former category, recent Stefan-type investigations have posed a variety of convective and radiative conditions at the upper and lower boundaries. Series expansion [16], similarity solution [23, 26], Laplace transform [20, 25], and Green's function techniques [21] have been used to solve these problems. There have also been quasi-steady models [13, 14] which employ perturbation expansions in powers of a small parameter, which is inversely proportional to the latent heat, and small in magnitude, due to the relatively large value of the latent heat. These one-dimensional analyses have generally investigated pure-systems, rather than alloy systems.

The two-dimensional analytical models incorporate side-wall heat transfer and lead to more realistic nonplanar solidification fronts. It is generally believed that one wishes to set the processing conditions to minimize front curvature so as to minimize transverse temperature gradients (hence, thermal stresses) and solute segregation. These two-dimensional models give some insight into the interplay between transverse and axial heat transfer in establishing the front shape. For Ohno casting, these issues are more relevant for the core fiber than the protective cladding, since the fiber quality is of primary interest. Brattkus and Davis [33] used a very successful steady-state asymptotic approach to investigate two-dimensional solidification. This approach consisted of expansions in a small aspect ratio, and a boundary layer analysis near the solidification front. The method has been employed successfully in pure and alloy systems, because most processing configurations seem to be characterized by a small aspect ratio. This approach is readily adaptable to ampoule and containerless geometries [39, 40]. The analysis which follows also makes use of this approach.

2. Derivation of the model and nondimensionalization

2.1. Assumptions

We make the simplifying assumption that the mandrel has zero thickness, and seek steady-state solutions. The system is assumed to be axisymmetric with respect to the horizontal midline in the core, denoted in Figure 2 as $\hat{r} = 0$. Our approach is to use asymptotic methods to reduce the steady-state, coupled set of partial differential equations, which govern the heat transfer in the cladding and core, to a coupled set of ordinary differential equations. Following [33, 39, 40], we accomplish this by taking advantage of the disparity between radial and

axial length scales. We define a melt slenderness ratio, $\varepsilon = \hat{R}_C/\hat{M}$, where $\hat{R}_C$ is the radius of the cladding and $\hat{M}$ is the length of the mold region. Here, ε is the small parameter in our asymptotic expansions. For the data listed in Table 1, $\varepsilon = 0{\cdot}125$. To assess the range of validity for our results will require a comparison with numerical simulations and experimental data. We are unaware of any such simulations or data for a cored rod system. However, [2, 5] present results for a single material rod system. They calculate isotherms, parabolic in shape, which appear to be in agreement with our analysis. They also conclude for small ε systems, that two-dimensional models give quite reasonable results. Furthermore, they find that buoyancy driven convection in the melt has a negligible effect on system heat transfer in small ε systems. This is because the Grashof number $O(10^2)$ is below critical due to the thin domain and relatively small difference between the input melt temperature and melting points of the core and cladding. Hence, we neglect buoyancy-driven convection in the analysis to follow. Thus, the melt motion is due solely to the forced input flow and conservation of mass caused by the pulling of the solidified rod.

Finally, we neglect thermal contraction of the metals after solidification and assume perfect thermal contact between the cladding and mold and between the cladding and core. A more complex model is required to include possible air gap formation and subsequent reduction of heat transfer due to contraction upon cooling. This is an area of extensive research in conventional casting [44–57].

Table 1. Input data

Parameter	Value	Units	Parameter	Value	Units
T_{C_M}	505·06	K	k_{SR}	0·5	$\mathrm{W\,cm^{-1}\,K^{-1}}$
T_{R_M}	456·16	K	V	18	$\mathrm{mm\,min^{-1}}$
T_{exit}	513	K	h_C^*	0·75	$\mathrm{W\,cm^{-2}\,K^{-1}}$
θ_{hot}	535	K	h_a^*	0·1	$\mathrm{W\,cm^{-2}\,K^{-1}}$
θ_{cold}	295	K	h_{SC}^*	0·75	$\mathrm{W\,cm^{-2}\,K^{-1}}$
$\hat{R}_r$	2·5	mm	L_{p_C}	17·6	$\mathrm{kJ\,kg^{-1}}$
$\hat{R}_C$	5	mm	L_{p_R}	19·59	$\mathrm{kJ\,kg^{-1}}$
$\hat{M}$	40	mm	$\hat{L}$	60	mm
a	1	–	$\hat{W}$	70	mm
b	0·22142	–	κ_C	0·1827	$\mathrm{cm^2\,s^{-1}}$
θ_0	0	–	κ_R	0·43313	$\mathrm{cm^2\,s^{-1}}$
$\tilde{f}$	2·133	–	κ_{SC}	0·38318	$\mathrm{cm^2\,s^{-1}}$
$\tilde{d}$	−6·933	–	κ_{SR}	0·46140	$\mathrm{cm^2\,s^{-1}}$
$\tilde{e}$	5·6			–	
k_C	0·326	$\mathrm{W\,cm^{-1}\,K^{-1}}$			
k_{SC}	0·607	$\mathrm{W\,cm^{-1}\,K^{-1}}$			
k_R	0·5	$\mathrm{W\,cm^{-1}\,K^{-1}}$			

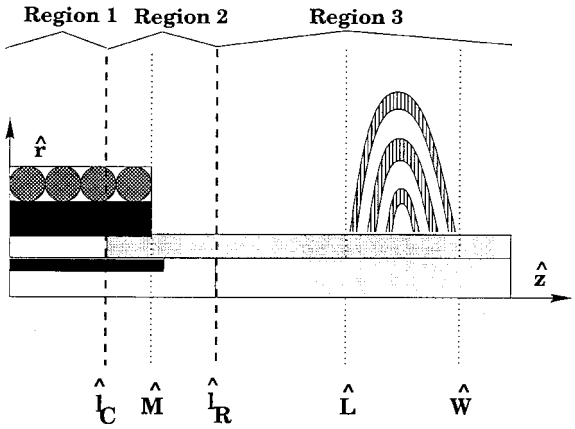

Figure 3. Region definitions.

Thus, using small ε and given the rod casting velocity V the input clad and core melt temperatures, the external temperatures, and the material properties, we derive approximate analytical solutions for the temperature fields in the cladding and core, as well as for the shapes of the solidifying clad and core interfaces. These solutions help to describe the parametric dependencies within the Ohno casting system.

2.2. Governing equations

Since there are different regions to be considered, the following subscripts will be used. A subscript of C will denote any quantity relating to the clad region. An R will denote the core region and S denotes a solid substance. A '$\hat{}$' denotes a dimensional quantity. In the analysis to follow the solidifying free boundaries will be defined by

$$\hat{h}(r) = \hat{l}_C + \hat{H}(r) \tag{2.1}$$

for the cladding, and

$$\hat{g}(r) = \hat{l}_R + \hat{G}(r) \tag{2.2}$$

for the core region. The unknown constants $\hat{l}_R$ and $\hat{l}_C$ are the mean positions of the interfaces, as shown in Figure 3. The unknown functions $\hat{H}(r)$ and $\hat{G}(r)$ represent the deviations from planarity.

In order to take advantage of a small melt slenderness ratio (melt radius/melt length), we scale the radial coordinates by $\hat{R}_C$ and the axial coordinates by $\hat{M}$. Thus, we let

$$\begin{aligned} &\hat{z} = \hat{M}z, \qquad \hat{r} = \hat{R}_C r, \qquad \hat{h} = \hat{M}h, \qquad \hat{g} = \hat{M}g, \\ &\hat{l}_C = \hat{M}l_C, \qquad \hat{l}_R = \hat{M}l_R, \qquad \hat{H} = \hat{R}_C H, \qquad \hat{G} = \hat{R}_C G. \end{aligned} \tag{2.3}$$

Temperature fields are scaled as follows:

$$\hat{T}_i = (\theta_{\text{hot}} - \theta_{\text{cold}})T_i + \theta_{\text{cold}}, \tag{2.4}$$

where θ_{hot} is the input melt temperature and θ_{cold} is the far field ($\hat{z} \to \infty$) temperature. We scale the melt velocities by the draw rate V.

The nondimensional governing equations are

$$\varepsilon^2 \,\mathrm{Pe}_C V_C T_{C_z} = T_{C_{rr}} + \frac{1}{r} T_{C_r} + \varepsilon^2 T_{C_{zz}}, \qquad 0 \leqslant z \leqslant h(r),\ R_r \leqslant r \leqslant 1, \tag{2.5}$$

$$\varepsilon^2 \,\mathrm{Pe}_R V_R T_{R_z} = T_{R_{rr}} + \frac{1}{r} T_{R_r} + \varepsilon^2 T_{R_{zz}}, \qquad 0 \leqslant z \leqslant g(r),\ 0 \leqslant r \leqslant R_r, \tag{2.6}$$

$$\varepsilon^2 \,\mathrm{Pe}_{SC} T_{SC_z} = T_{SC_{rr}} + \frac{1}{r} T_{SC_r} + \varepsilon^2 T_{SC_{zz}}, \qquad h(r) \leqslant z < \infty,\ R_r \leqslant r \leqslant 1, \tag{2.7}$$

$$\varepsilon^2 \,\mathrm{Pe}_{SR} T_{SR_z} = T_{SR_{rr}} + \frac{1}{r} T_{SR_r} + \varepsilon^2 T_{SR_{zz}}, \qquad g(r) \leqslant z < \infty,\ 0 \leqslant r \leqslant R_r, \tag{2.8}$$

where Pe_C, Pe_R, Pe_{SC}, and Pe_{SR} are the Peclet numbers for the various materials. The Peclet number is defined to be $\mathrm{Pe}_i = V\hat{M}/\kappa_i$, for the different values of the thermal diffusivity, κ_i, $i = C, R, SC, SR$. Since the Peclet numbers are on the order of 10^{-1} in magnitude, the heat transfer is conduction-dominated.

Due to the small ε approximation and low Reynolds number, the melt flow profiles will be fully developed away from the entrance region and away from the interface locations at l_C and l_R. Hence, in Equations (2.5) and (2.6) we include only the axial melt velocities V_C and V_R. Assuming the input melt velocities are uniform flows with speed V, we write the velocity profiles V_C and V_R in the form $V_i(r) = \tilde{V}_i(r) + 1$ with

$$\int_{R_r}^{1} \tilde{V}_C r \,\mathrm{d}r = 0, \qquad \int_{0}^{R_r} \tilde{V}_R r \,\mathrm{d}r = 0 \tag{2.9}$$

by conservation of mass. Further, we expect $\tilde{V}_R = 0$ after the mandrel ends, since the core interface solidifies with rate V and the solid cladding moves at this same speed.

2.3. Boundary conditions

In determining the boundary conditions, it is necessary to divide the system into three regions, each with one or more sections. The region divisions are at critical values of $\hat{z}$. This scheme is illustrated in Figure 3.

The boundary conditions at the centerline, $r = 0$, are

$$T_{R_r} = 0,\ T_{SR_r} = 0. \tag{2.10}$$

At $r = R_r$, $R_r = \hat{R}_r/\hat{R}_C$, we impose continuity of heat flux and temperature,

$$\frac{k_C}{k_R} T_{C_r} = T_{R_r},\ T_C = T_R, \qquad \text{in region 1, } (0 \leqslant z \leqslant h(R_r)) \tag{2.11}$$

$$\frac{k_C}{k_R} T_{SC_r} = T_{R_r},\ T_{SC} = T_R, \qquad \text{in region 2, } (h(R_r) \leqslant z \leqslant g(R_r)) \tag{2.12}$$

$$\frac{k_{SC}}{k_{SR}} T_{SC_r} = T_{SR_r},\ T_{SC} = T_{SR}, \qquad \text{in region 3, } (g(R_r) \leqslant z < \infty). \tag{2.13}$$

Here, k_i, $i = C, R, SC, SR$, denotes the thermal conductivities.

Along $r = 1$, the boundary of the clad region, we have the energy balance for heat transfer between the liquid and solid clad regions and the surrounding environment. This is defined by

$$T_{C_r} = \beta_C(\Theta(z) - T_C), \tag{2.14}$$

$$T_{SC_r} = \beta_{SC}(\Theta(z) - T_{SC}), \tag{2.15}$$

where $\beta_C = h_C^* \hat{R}_C / k_C$ and,

$$\beta_{SC} = \begin{cases} \dfrac{h_C^* \hat{R}_C}{k_{SC}} & \text{if } l_C < z < 1 \\ \dfrac{h_{SC}^* \hat{R}_C}{k_{SC}} & \text{if } L < z < W \\ \dfrac{h_a^* \hat{R}_C}{k_{SC}} & \text{if } 1 < z < L, z > W \end{cases} \tag{2.16}$$

are the Biot numbers. h_C^*, h_{SC}^* and h_a^* represent the heat transfer coefficients between the solid cladding and mold, water spray, and air, respectively. $\Theta(z)$ is a function that describes the outer temperature field. This temperature field is a piecewise function on the interval $z \in [0, \infty)$. It describes the temperature in the heated mold, followed by the air cooling zone, the water spray zone and then the final air zone. The definition of $\Theta(z)$ will be given shortly. We note that radiation is negligible, due to the low surface temperatures [5]. In Equation (2.16) we set different definitions of the Biot number for the zones shown in Figure 3. These zones represent heat transfer between the solid cladding and mold ($l_C < z < 1$), between the solid cladding and water spray ($L < z < W$), and between the solid cladding and air ($1 < z < L, z > W$). This is consistent with the findings in [5]. While [5] presents a continuous model for the variation of the heat transfer coefficient over the zones, we use averaged values of the data in [5] to define the constant heat transfer coefficients in each zone, as listed in Table 1.

Further, by taking these Biot numbers as $O(1)$ quantities in the analysis to follow, we find that perfect heat transfer occurs along the boundaries. Hence, the temperature of the rod becomes identical to the imposed external temperature profile under the steady state assumption. Thus we pose that the Biot numbers are $O(\varepsilon^2)$ quantities, *i.e.*,

$$\beta_C = \varepsilon^2 \overline{\beta_C}, \quad \beta_{SC} = \varepsilon^2 \overline{\beta_{SC}}. \tag{2.17}$$

This scaling is not necessarily satisfied by the data listed in Table 1. However, [5] presents a comparison between numerical simulations and a one-dimensional control volume approach, derived under the assumption of a small Biot number. This comparison demonstrates that the control volume model leads to reasonable predictions for the thermal profile in slender rods given by the data in Table 1. Hence, we pose Equation (2.17) and follow the asymptotic analysis of directional solidification systems for small aspect ratio domains presented in [33, 39, 40]. We note that a similar asymptotic procedure, also relevant for small surface heat transfer, is presented in [58, 59]. In this procedure, the asymptotic expansions are developed in the limit of a small surface heat transfer parameter. We could have recast our model into

this framework. In this context the data in Table 1 results in a *large* small parameter. Nevertheless, our conjecture is that it is reasonable to proceed with these small surface heat transfer approaches, based upon the comparison in [5].

In essence, the scaling in Equation (2.17) leads to a balance between axial and radial heat transfer in Equations (2.5)–(2.8) at $O(\varepsilon^2)$. Thus, Equations (2.14)–(2.15) become

$$T_{C_r} = \varepsilon^2 \overline{\beta_C}(\Theta(z) - T_C), \tag{2.18}$$

$$T_{SC_r} = \varepsilon^2 \overline{\beta_{SC}}(\Theta(z) - T_{SC}). \tag{2.19}$$

At $z = 0$ we have,

$$T_C = 1, \qquad T_R = 1. \tag{2.20}$$

As $z \to \infty$,

$$T_{SC} \to 0, \qquad T_{SR} \to 0. \tag{2.21}$$

At the solidifying core front, $z = g(r) = l_R + \varepsilon G(r)$, we have,

$$T_R = T_{R_M} = T_{SR}, \tag{2.22}$$

and at the solidifying clad front, $z = h(r) = l_C + \varepsilon H(r)$, we have

$$T_C = T_{C_M} = T_{SC}. \tag{2.23}$$

Here T_{C_M} and T_{R_M} are the scaled melting points. Energy balances at these fronts are given by

$$K_C(\varepsilon T_{SC_z} - T_{SC_r} H_r) - (\varepsilon T_{C_z} - T_{C_r} H_r) = -\varepsilon \,\mathrm{St}_C \,\mathrm{Pe}_C, \tag{2.24}$$

$$K_R(\varepsilon T_{SR_z} - T_{SR_r} G_r) - (\varepsilon T_{R_z} - T_{R_r} G_r) = -\varepsilon \,\mathrm{St}_R \,\mathrm{Pe}_R, \tag{2.25}$$

where, $K_C = k_{SC}/k_C$, $K_R = k_{SR}/k_R$, and $\mathrm{St}_C = L_{pC}/c_{pC}\Delta T$, $\mathrm{St}_R = L_{pR}/c_{pR}\Delta T$ are the Stefan numbers. The constants c_{pC} and c_{pR} are the specific heats, and $\Delta T = \theta_{\text{hot}} - \theta_{\text{cold}}$. L_{pC}, L_{pR} denote latent heats per unit volume.

Two other equations are obtained from integrating Equations (2.1) and (2.2),

$$\int_{R_r}^{1} H(r) r \, \mathrm{d}r = 0, \tag{2.26}$$

$$\int_{0}^{R_r} G(r) r \, \mathrm{d}r = 0. \tag{2.27}$$

These equations are needed since both the mean value positions and the deviations from planarity are unknown.

3. Asymptotic analysis

As in [33, 39, 40], we expect boundary layers to appear near the interfaces between the liquid and solid phases. In these regions, the axial and radial heat transfers balance to set the shape of the solidifying fronts.

3.1. The outer problem

The outer problem occurs in the regions away from the solidification fronts. We assume straight forward asymptotic expansions for the temperatures. These are defined as follows

$$T_i = T_{i_0} + \varepsilon T_{i_1} + \varepsilon^2 T_{i_2} + \cdots, \tag{3.1}$$

where $i = C, R, SC, SR$ and each of the subscripted temperature quantities are functions of r and z. Also, at the interfaces, we assume the asymptotic expansions

$$\begin{aligned} H(r) &= \varepsilon H_0 + \varepsilon^2 H_1 + \varepsilon^3 H_2 + \cdots, \\ G(r) &= \varepsilon G_0 + \varepsilon^2 G_1 + \varepsilon^3 G_2 + \cdots. \end{aligned} \tag{3.2}$$

These orders, the nondimensionalized versions of $h(r)$ and $g(r)$, and scalings in Equations (2.17) are consistent with the above discussion concerning axial and radial heat transfer balance. It will be shown in the analysis to follow, that radial heat transfer appears at $O(\varepsilon^2)$. Because of the axially dominated heat conduction, the interfaces are nearly flat, as described by the ordering in Equation (3.2).

Substituting the above expansions in the governing Equation (2.6) in the liquid core region we find, at $O(1)$,

$$T_{R_0}(r, z) = A_{R_0}(z) \log(r) + B_{R_0}(z), \tag{3.3}$$

where $A_{R_0}(z)$ and $B_{R_0}(z)$ are unknown functions to be determined by the boundary conditions. From (2.10), it follows that

$$T_{R_0}(r, z) = B_{R_0}(z). \tag{3.4}$$

Similarly, at $O(\varepsilon)$, we find that

$$T_{R_1}(r, z) = B_{R_1}(z), \tag{3.5}$$

where $B_{R_1}(z)$ is also unknown.

At $O(\varepsilon^2)$ the governing equation is

$$T_{R_{2_{rr}}} + \frac{1}{r} T_{R_{2_r}} = -(T_{R_{0_{zz}}} - \mathrm{Pe}_R(\tilde{V}_R(r) + 1) T_{R_{0_z}}). \tag{3.6}$$

Upon integration, we find that

$$T_{R_2}(r, z) = -\frac{r^2}{4}(B''_{R_0} - \mathrm{Pe}_R B'_{R_0}) + \mathrm{Pe}_R B'_{R_0} \int_0^r \frac{1}{x} \int_0^x \tilde{V}_R(y) y \, \mathrm{d}y \, \mathrm{d}x + B_{R_2}(z), \tag{3.7}$$

where $'$ denotes differentiation with respect to z, and we have used (3.4) and a boundedness criterion. Further, $B_{R_2}(z)$ is another unknown function of z. A similar solution process in the liquid clad region gives

$$T_{C_0}(r,z) = B_{C_0}(z), \tag{3.8}$$

$$T_{C_1}(r,z) = B_{C_1}(z), \tag{3.9}$$

$$\begin{aligned} T_{C_2}(r,z) \;=\; & \left(-\frac{r^2}{4} + \frac{1}{2}\log(r)\right)(B''_{C_0} - \mathrm{Pe}_C B'_{C_0}) + \log(r)\overline{\beta_C}(\Theta(z) - B_{C_0}) \\ & + \mathrm{Pe}_C B'_{C_0} \int_{R_r}^{r} \frac{1}{x} \int_{R_r}^{x} \tilde{V}_C(y)\, y \,\mathrm{d}y \,\mathrm{d}x + B_{C_2}, \end{aligned} \tag{3.10}$$

where we have used Equation (2.18), and where B_{C_i}, $i = 0, 1, 2$ are all unknown functions of z.

The solutions in the solid regions are determined in similar fashion, and found to be:

$$T_{SR_0}(r,z) = B_{SR_0}(z), \tag{3.11}$$

$$T_{SR_1}(r,z) = B_{SR_1}(z), \tag{3.12}$$

$$T_{SR_2}(r,z) = -\frac{r^2}{4}(B''_{SR_0} - \mathrm{Pe}_{SR} B'_{SR_0}) + B_{SR_2}(z), \tag{3.13}$$

$$T_{SC_0}(r,z) = B_{SC_0}(z), \tag{3.14}$$

$$T_{SC_1}(r,z) = B_{SC_1}(z), \tag{3.15}$$

$$\begin{aligned} T_{SC_2}(r,z) \;=\; & \left(-\frac{r^2}{4} + \frac{1}{2}\log(r)\right)(B''_{SC_0} - \mathrm{Pe}_{SC} B'_{SC_0}) \\ & + \log(r)\overline{\beta_{SC}}(\Theta(z) - B_{SC_0}) + B_{SC_2}. \end{aligned} \tag{3.16}$$

Again, the terms B_{SR_i} and B_{SC_i} are unknown functions of z. We have not yet used the temperature and heat flux conditions (2.11–2.13). At $O(1)$, (2.11) implies that

$$B_{R_0}(z) = B_{C_0}(z). \tag{3.17}$$

At $O(\varepsilon)$, we have

$$B_{R_1}(z) = B_{C_1}(z), \tag{3.18}$$

and at $O(\varepsilon^2)$, the two conditions yield the following ODE for $B_{C_0}(z)$,

$$B''_{C_0} - B_1 B'_{C_0} - C_1 B_{C_0} = -C_1 \Theta(z), \tag{3.19}$$

where

$$B_1 = -\frac{R_r^2(-k_C\,\mathrm{Pe}_C + k_R\,\mathrm{Pe}_R) + k_C\,\mathrm{Pe}_C}{R_r^2(k_C - k_R) - k_C}, \tag{3.20}$$

$$C_1 = -\frac{2k_C\bar{\beta}_C}{R_r^2(k_C - k_R) - k_C}.$$

In the above, we have used Equation (2.9). Hence, in this solution procedure, the details of the fully developed flow are averaged out over the radial direction and the system responds as if the melt velocity is a uniform flow with speed V. For this reason, we shall ignore the flow details in the remainder of this analysis, and assume uniform melt velocities in the core and clad melt. Thus, Equation (3.19), defining the leading order temperature field in this asymptotic approach, is the type of one-dimensional equation one derives when performing a heat balance using a control volume approach [5]. However, the asymptotic framework presented here allows one to derive two-dimensional corrections. We shall comment on the range of validity of the leading order one-dimensional approximation below. For region 2, as in Figure 3, the set of boundary conditions (2.12, 2.19) produce a similar ODE for B_{SC_0}

$$B''_{SC_0} - B_2 B'_{SC_0} - C_2 B_{SC_0} = -C_2\Theta(z) \tag{3.21}$$

where

$$B_2 = -\frac{R_r^2(-k_{SC}\,\mathrm{Pe}_{SC} + k_R\,\mathrm{Pe}_R) + k_{SC}\,\mathrm{Pe}_{SC}}{R_r^2(k_{SC} - k_R) - k_{SC}}, \qquad C_2 = -\frac{2k_{SC}\bar{\beta}_{SC}}{R_r^2(k_{SC} - k_R) - k_{SC}}. \tag{3.22}$$

Finally, in region 3, Equations (2.13, 2.19) yield

$$B''_{SC_0} - B_3 B'_{SC_0} - C_3 B_{SC_0} = -C_3\Theta(z), \tag{3.23}$$

$$B_3 = -\frac{R_r^2(-k_{SC}\,\mathrm{Pe}_{SC} + k_{SR}\,\mathrm{Pe}_{SR}) + k_{SC}\,\mathrm{Pe}_{SC}}{R_r^2(k_{SC} - k_{SR}) - k_{SC}}, \tag{3.24}$$

$$C_3 = -\frac{2k_{SC}\bar{\beta}_{SC}}{R_r^2(k_{SC} - k_{SR}) - k_{SC}}.$$

The constants C_i and B_i in Equations (3.20, 3.22 and 3.24) represent conduction-averaged Peclet and Biot numbers, respectively. Hence, the system behaves as if the cladding and core combination has been replaced by a single material with the effective properties defined by these constants.

In the previous equations, (3.19), (3.21) and (3.23), the forcing term $\Theta(z)$ describes the temperature field outside the rod. We define $\Theta(z)$ piecewise as follows

$$\Theta(z) = \begin{cases} a + bz, & 0 < z < 1 \\ \theta_0, & 1 < z < L \\ \tilde{f}z^2 + \tilde{d}Z + \tilde{e}, & L < z < W \\ \theta_0, & W < z < \infty, \end{cases} \tag{3.25}$$

where $a, b, \theta_0, \tilde{f}, \tilde{d}$, and $\tilde{e}$ are all constants listed in Table 1. The four zones of $\Theta(z)$ represent a linearly decreasing temperature field in the mold region [2, 5], the ambient air temperature θ_0 between the mold and water spray, the water spray temperature, and the ambient zone after the water spray. The parabolic model in the water spray is used to simulate variable heat transfer in this region [5]. In dimensional units, the water spray changes from 23°C at $z = L$ and $z = W$, to 14°C at the midpoint between L and W.

The solutions of Equations (3.19, 3.21, 3.23) provide the leading order temperature profiles. These one-dimensional approximations will be valid, provided the radially dependent correction terms in Equations (3.7, 3.10, 3.13, 3.16) are small in comparison to these approximations. As a crude estimate of such a comparison, we consider the limiting case of equal thermal conductivities. Thus, the C_i and B_i in Equations (3.20, 3.22, and 3.24) reduce to Peclet numbers and Biot numbers, respectively. The coefficients of the radially dependent terms in Equations (3.7, 3.10, 3.13, 3.16) are then related to the third and fourth terms in Equations (3.19, 3.21, 3.23). Hence, it can be shown that the radially dependent correction terms are small in comparison to the leading order one-dimensional temperature fields provided that $\beta_i(\Theta(z) - B_i)/2B_i \ll 1$, $i = S, SC$, which means that the radial heat transfer is small in Equations (2.14, 2.15). In deriving the above, we have used Equation (2.17). For Ohno casting, the comparison between the ambient temperature and the temperature of the rods satisfies $(\Theta(z) - B_i)/B_i < 1$, by design. Thus, the one-dimensional approximation is valid for $\beta_i \ll 2$. This is satisfied for the data in Table 1, although Equation (2.17) is not necessarily satisfied. Hence, the validity of the one-dimensional approximation extends somewhat beyond this strict ordering. We also point out that if the Biot numbers are large, then the constants C_i, $i = 1, 2, 3$ are large. Hence, the Equations (3.19), (3.21) and (3.23) lead to solutions where the temperature fields approach $\Theta(z)$. This is consistent with the earlier discussion concerning the orders of approximation given in Equation (2.17).

In region 1, $0 < z < l_C$, the governing ODE is (3.19). The boundary conditions are

$$B_{C_0}(0) = 1, \; B_{C_0}(l_c) = T_{C_M}. \tag{3.26}$$

The former follows from Equation (2.20), and the latter from (2.23). This ODE is solved to obtain

$$B_{C_0}(z) = \varphi_1 \, \mathrm{e}^{n_1 z} + \varphi_2 \, \mathrm{e}^{n_2 z} + y_1 + y_2 z \tag{3.27}$$

where

$$\begin{aligned} n_1 &= \frac{B_1 + \sqrt{B_1^2 + 4C_1}}{2}, \quad n_2 = \frac{B_1 - \sqrt{B_1^2 + 4C_1}}{2}, \\ y_1 &= \frac{a + B_1 b}{c_1}, \quad y_2 = b, \\ \varphi_1 &= \frac{(1 - y_1)\,\mathrm{e}^{n_2 l_C} - (T_{C_M} - y_1 - y_2 l_C)}{\mathrm{e}^{n_2 l_C} - \mathrm{e}^{n_1 l_C}}, \quad \varphi_2 = \frac{(T_{C_M} - y_1 - y_2 l_C) - (1 - y_1)\,\mathrm{e}^{n_1 l_C}}{\mathrm{e}^{n_2 l_C} - \mathrm{e}^{n_1 l_C}}. \end{aligned} \tag{3.28}$$

Referring to Figure 3 and the piecewise definition of $\Theta(z)$ in Equation (3.25), we solve Equations (3.21) and (3.23) by splitting these equations into five zones: $l_C < z < 1$, $1 < z < l_R$, $l_R < z < L$, $L < z < W$, and $W < z < \infty$. We refer to the solutions in these zones

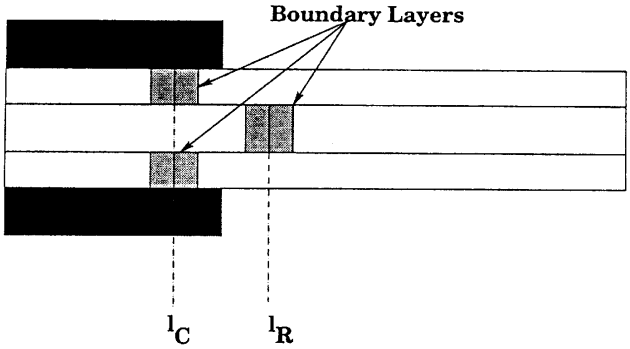

Figure 4. Boundary layers.

as $B_{SC_0}^{(2.1)}$, $B_{SC_0}^{(2.2)}$, $B_{SC_0}^{(3.1)}$, $B_{SC_0}^{(3.2)}$, $B_{SC_0}^{(3.3)}$, respectively. Continuity of temperature and heat flux are used as the boundary conditions at $z = 1$ (the mold exit), and at $z = L$ (the water spray zone). At $z = l_C$ we impose the condition $B_{SC_0}^{(2.1)} = T_{C_M}$, at $z = l_R$ we impose $B_{SC_0}^{(2.2)} = T_{R_M} = B_{SC_0}^{(3.1)}$. These are derived using (2.22) and (2.23). As $z \to \infty$ we use $B_{SC_0}^{(3.3)} = 0$ which follows from Equation (2.21). The details of the solution can be found in [60]. We note that the forms of the ODE solutions are similar to Equation (3.27) and that the constants (such as φ_1 and φ_2 in Equation (3.27)) are functions of l_C and l_R, the mean positions of the solidification fronts. These positions are still unknown and are determined in the boundary layer analysis to follow.

3.2. THE INNER PROBLEM

The inner problem deals with the areas close to the interfaces, as shown in Figure 4. In these regions, we have not yet satisfied the latent heat equations (2.24, 2.25). At this point, one could substitute the leading-order temperature fields in Equations (2.24, 2.25) and develop coupled equations for the mean interface locations, l_C and l_R. However, determination of the non-planar corrections, $H(r)$ and $G(r)$, requires a boundary-layer analysis. Hence, we define two boundary layer coordinates, $\xi = z - l_c/\varphi(\varepsilon)$ and $\eta = z - l_R/\psi(\varepsilon)$.

Note that in Figure 3, region 1, $\xi \to -\infty$ to the left of the boundary layer at $z = l_C$, and in region 2, $\xi \to \infty$ to the right of the boundary layer; η behaves similarly in region 2 near $z = l_R$. The boundary layers appear in both the clad and core regions, so there are four temperatures we must resolve near each boundary layer. We define $\tilde{T}_C$ and $\tilde{T}_{SC}$ to be the boundary-layer temperatures in the cladding and $\tilde{T}_R$ and $\tilde{T}_{SR}$ in the core region. We find that $\varphi(\varepsilon)$, and $\psi(\varepsilon)$, the boundary-layer thicknesses, are both of order $O(\varepsilon)$, which allows us to retain the axial heat transfer terms in Equations (2.5–2.8). We then pose,

$$\tilde{T}_i = \tilde{T}_{i_0} + \varepsilon \tilde{T}_{i_1} + \varepsilon^2 \tilde{T}_{i_2} + \cdots, \tag{3.29}$$

where $i = C, R, SC, SR$.

First we examine the boundary layer near l_C. We adopt a superscript notation denoting the region that the particular temperature is associated with (1 for region 1, etc.). Equations (2.5) through (2.8) become,

$$\tilde{T}_{R_{rr}}^{(1)} + \frac{1}{r}\tilde{T}_{R_r}^{(1)} + \tilde{T}_{R_{\xi\xi}}^{(1)} = \varepsilon \,\mathrm{Pe}_R \tilde{T}_{R_\xi}^{(1)}, \tag{3.30}$$

$$\tilde{T}^{(2)}_{R_{rr}} + \frac{1}{r}\tilde{T}^{(2)}_{R_r} + \tilde{T}^{(2)}_{R_{\xi\xi}} = \varepsilon \,\mathrm{Pe}_R \tilde{T}^{(2)}_{R_\xi}, \tag{3.31}$$

$$\tilde{T}_{C_{rr}} + \frac{1}{r}\tilde{T}_{C_r} + \tilde{T}_{C_{\xi\xi}} = \varepsilon \,\mathrm{Pe}_C \tilde{T}_{C_\xi}, \tag{3.32}$$

$$\tilde{T}^{(2)}_{SC_{rr}} + \frac{1}{r}\tilde{T}^{(2)}_{SC_r} + \tilde{T}^{(2)}_{SC_{\xi\xi}} = \varepsilon \,\mathrm{Pe}_{SC} \tilde{T}^{(2)}_{SC_\xi}, \tag{3.33}$$

In the above we have assumed a uniform melt velocity, as discussed in the outer problem. While this is not actually the case, due to no-slip along the mold and mandrel walls, we impose this condition for simplicity.

We list only those boundary conditions that are referred to in the analysis to follow.

At the solidification front, $\xi = \varepsilon H(r)$, we have the conditions,

$$\tilde{T}^{(1)}_{R_r} = \tilde{T}^{(2)}_{R_r}, \tilde{T}^{(1)}_{R} = \tilde{T}^{(2)}_{R}, \tag{3.34}$$

$$\tilde{T}_C = T_{C_M} = \tilde{T}^{(2)}_{SC}, \tag{3.35}$$

$$K_C(\tilde{T}^{(2)}_{SC_\xi} - \tilde{T}^{(2)}_{SC_r} H_r) - (\tilde{T}_{C_\xi} - \tilde{T}_{C_r} H_r) = -\varepsilon \,\mathrm{St}_C \mathrm{Pe}_C. \tag{3.36}$$

Finally, we have the matching conditions,

$$\begin{aligned} &\lim_{\xi\to-\infty}(T_R - \tilde{T}^{(1)}_R) = 0, \qquad \lim_{\xi\to\infty}(T_R - \tilde{T}^{(2)}_R) = 0, \\ &\lim_{\xi\to-\infty}(T_C - \tilde{T}_C) = 0, \qquad \lim_{\xi\to\infty}(T_{SC} - \tilde{T}^{(2)}_{SC}) = 0. \end{aligned} \tag{3.37}$$

Similarly, in the boundary layer region near $z = l_R$, we assume a uniform melt velocity as in the outer problem discussion. Near l_R, this is reasonable, since the solidification rate is V and since the solid clad moves at this same velocity. The governing equations are then similar to those listed near l_C. At the solidification front, $\eta = \varepsilon G(r)$, we have

$$\tilde{T}^{(2)}_{SC_r} = \tilde{T}^{(3)}_{SC_r}, \tilde{T}^{(2)}_{SC} = \tilde{T}^{(3)}_{SC}, \tag{3.38}$$

$$\tilde{T}^{(2)}_R = T_{R_M} = \tilde{T}_{SR}, \tag{3.39}$$

$$K_R(\tilde{T}_{SR_\eta} - \tilde{T}_{SR_r} G_r) - (\tilde{T}^{(2)}_{R_\eta} - \tilde{T}^{(2)}_{R_r} G_r) = -\varepsilon \,\mathrm{St}_R \,\mathrm{Pe}_R. \tag{3.40}$$

Finally, we have the matching conditions,

$$\begin{aligned} &\lim_{\eta\to-\infty}(T_R - \tilde{T}^{(2)}_R) = 0, \qquad \lim_{\eta\to\infty}(T_{SR} - \tilde{T}_{SR}) = 0, \\ &\lim_{\eta\to-\infty}(T_{SC} - \tilde{T}^{(2)}_{SC}) = 0, \qquad \lim_{\eta\to\infty}(T_{SC} - \tilde{T}^{(3)}_{SC}) = 0. \end{aligned} \tag{3.41}$$

The matching conditions (3.37) and (3.41) require the outer solutions. Substituting Equations (3.4), (3.5), and (3.7), in (3.1) we find that

$$T_R(r,z) = B_{R_0}(z) + \varepsilon B_{R_1}(z) + \varepsilon^2\left[-\frac{r^2}{4}(B''_{R_0} - \mathrm{Pe}_R B'_{R_0}) + B_{R_2}(z)\right] + \cdots. \tag{3.42}$$

Similar expressions are developed for $T_C(r, z)$, $T_{SR}(r, z)$, and $T_{SC}(r, z)$. The matching process requires that we write these outer solutions in terms of the inner variables, ξ and η. Using Equation (3.42), we have that in the liquid core.

$$T_R = B_{R_0}(l_C) + \varepsilon(B_{R_1}(l_C) + \xi B'_{R_0}(l_C)) + \varepsilon^2 \left[B_{R_2}(l_C) + \varepsilon B'_{R_1}(l_C) + \frac{\xi^2}{2} B''_{R_0}(l_C) - \frac{r^2}{4}(B''_{R_0}(l_C) - \mathrm{Pe}_R\, B'_{R_0}(l_C)) \right] + \cdots. \tag{3.43}$$

This can be repeated with the other temperature fields near $z = l_C$ and $z = l_R$. From here one can determine the matching conditions at various orders.

The solutions to the leading-order boundary-layer problem near $z = l_C$ are given by

$$\tilde{T}^{(1)}_{R_0} = \tilde{T}^{(2)}_{R_0} = B_{R_0}(l_C), \tag{3.44}$$

$$\tilde{T}_{C_0} = \tilde{T}^{(2)}_{SC_0} = B_{C_0}(l_C) = B_{SC_0}(l_C) = T_{C_M}. \tag{3.45}$$

Via a similar analysis at the boundary layer near $z = l_R$ we find, using the leading order, that

$$\tilde{T}^{(2)}_{R_0} = \tilde{T}_{SR_0} = B_{R_0}(l_R) = B_{SR_0}(l_R) = T_{R_M}, \tag{3.46}$$

$$\tilde{T}^{(2)}_{SC_0} = \tilde{T}^{(3)}_{SC_0} = B_{SC_0}(l_R). \tag{3.47}$$

Solving the $O(\varepsilon)$ problem, we find that

$$\tilde{T}^{(1)}_{R_1}(r, \xi) = \tilde{T}^{(2)}_{R_1}(r, \xi) = B'_{R_0}(l_C) \cdot \xi, \tag{3.48}$$

$$\tilde{T}_{C_1}(r, \xi) = B'_{C_0}(l_C) \cdot \xi, \tag{3.49}$$

$$\tilde{T}^{(2)}_{SC_1}(r, \xi) = B'_{SC_0}(l_C) \cdot \xi, \tag{3.50}$$

$$\tilde{T}^{(2)}_{R_1}(r, \eta) = B'_{R_0}(l_R) \cdot \eta, \tag{3.51}$$

$$\tilde{T}_{SR_1}(r, \eta) = B'_{SR_0}(l_R) \cdot \eta, \tag{3.52}$$

$$\tilde{T}^{(2)}_{SC_1}(r, \eta) = \tilde{T}^{(3)}_{SC_1}(r, \eta) = B'_{SC_0}(l_R) \cdot \eta. \tag{3.53}$$

For $O(\varepsilon)$, the latent heat conditions, Equations (3.36) and (3.40) become

$$K_C B^{(2.1)}_{SC_0}(l_C) - B'_{C_0}(l_C) = -\mathrm{St}_C\, \mathrm{Pe}_C, \tag{3.54}$$

$$K_R B^{(2.2)}_{SC_0}(l_R) - B'_{C_0}(l_R) = -\mathrm{St}_R\, \mathrm{Pe}_R. \tag{3.55}$$

Equations (3.54) and (3.55) are two coupled nonlinear equations for the mean solidifying positions l_C and l_R. The coupling occurs since the outer solutions for B_{C_0}, $B^{(2.1)}_{SC_0}$ and $B^{(2.2)}_{SC_0}$ are functions of both l_C and l_R, as discussed previously. Maple V was used to solve (3.54) and (3.55) for l_C and l_R. Contour plots of Equations (3.54) and (3.55) over an l_C and l_R

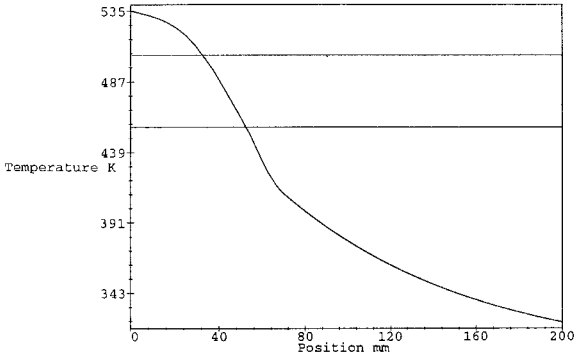

Figure 5. Temperature profile in the clad melt and solid regions.

neighborhood around the mold exit appear to reveal a unique solution in this region. For the data listed in Table 1, we find that $l_C = 0{\cdot}8088$ (32·352 mm), and $l_R = 1{\cdot}316$ (52·64 mm). A plot of the temperature profile found in the clad regions is plotted in Figure 5. Notice where the function intersects the two horizontal lines. The top line is the melting temperature of the clad region, and the bottom line is the melting point of the core. These intersection points represent the mean positions of the solidification fronts, l_C and l_R, respectively. Further discussion of these results will take place in the section on parametric studies which follows. As a final note, the above boundary layer analysis is not necessary if we are only interested in determining the mean planar locations. Equations (3.54) and (3.55) follow from (2.24) and (2.25), using a one-dimensional analysis. The boundary-layer discussion above is presented only as a consistent development for the next section.

3.3. Deviation from Planarity

Now that we have determined the mean positions of the interfaces, our focus is on determining the correction factors associated with each interfacial shape, *i.e.*, $H(r)$ and $G(r)$. We will accomplish this by continuing the asymptotic analysis to $O(\varepsilon^2)$, and making use of Equation (3.2).

In regions 1 and 2, we list some of the equations to be solved.

$$\tilde{T}^{(1)}_{R_{2rr}} + \frac{1}{r}\tilde{T}^{(1)}_{R_{2r}} + \tilde{T}^{(1)}_{R_{2\xi\xi}} = \mathrm{Pe}_R\, \tilde{T}^{(1)}_{R_{1_\xi}}, \tag{3.56}$$

$$\tilde{T}^{(2)}_{R_{2rr}} + \frac{1}{r}\tilde{T}^{(2)}_{R_{2r}} + \tilde{T}^{(2)}_{R_{2\xi\xi}} = \mathrm{Pe}_R\, \tilde{T}^{(2)}_{R_{1_\xi}}. \tag{3.57}$$

In order to simplify these and obtain a simpler version of the matching condition Equation (3.37) at $O(\varepsilon^2)$, we define the modified temperatures, $\bar{T}^{(1)}_R$ and $\bar{T}^{(2)}_R$ such that

$$\tilde{T}^{(1)}_{R_2}(r,\xi) = \frac{\xi^2}{2}B''_{R_0}(l_C) + \xi B'_{R_1}(l_C) + B_{R_2}(l_C) - \frac{r^2}{4}(B''_{R_0}(l_C) - \mathrm{Pe}_R B'_{R_0}(l_C)) + \bar{T}^{(1)}_R, \tag{3.58}$$

$$\tilde{T}^{(2)}_{R_2}(r,\xi) = \frac{\xi^2}{2}B''_{R_0}(l_C) + \xi B'_{R_1}(l_C) + B_{R_2}(l_C) - \frac{r^2}{4}(B''_{R_0}(l_C) - \mathrm{Pe}_R B'_{R_0}(l_C)) + \bar{T}^{(2)}_R. \tag{3.59}$$

The form of these substitutions is motivated by Equation (3.43) which is used in the matching process. Similarly, in the outer regions we develop expressions for $\tilde{T}_{C_2}(r,\xi)$, $\tilde{T}^{(2)}_{SC_2}(r,\xi)$, $\tilde{T}^{(2)}_{R_2}(r,\eta)$, $\tilde{T}_{SR_2}(r,\eta)$, $\tilde{T}^{(2)}_{SC_2}(r,\eta)$, and $\tilde{T}^{(3)}_{SC_2}(r,\eta)$.

By defining the solutions in this way, we develop the following set of equations for the modified temperatures $\bar{T}_i$. The equations near $z = l_C$ become

$$\bar{T}^{(1)}_{R_{rr}} + \frac{1}{r}\bar{T}^{(1)}_{R_r} + \bar{T}^{(1)}_{R_{\xi\xi}} = 0, \tag{3.60}$$

$$\bar{T}^{(2)}_{R_{rr}} + \frac{1}{r}\bar{T}^{(2)}_{R_r} + \bar{T}^{(2)}_{R_{\xi\xi}} = 0, \tag{3.61}$$

$$\bar{T}_{C_{rr}} + \frac{1}{r}\bar{T}_{C_r} + \bar{T}_{C_{\xi\xi}} = 0, \tag{3.62}$$

$$\bar{T}^{(2)}_{SC_{rr}} + \frac{1}{r}\bar{T}^{(2)}_{SC_r} + \bar{T}^{(2)}_{SC_{\xi\xi}} = 0, \tag{3.63}$$

subject to the matching conditions

$$\lim_{\xi\to-\infty} \bar{T}^{(1)}_R = \lim_{\xi\to\infty} \bar{T}^{(2)}_R = 0, \qquad \lim_{\xi\to-\infty} \bar{T}_C = \lim_{\xi\to\infty} \bar{T}^{(2)}_{SC} = 0. \tag{3.64}$$

As stated previously, the simplicity of the matching conditions motivates the change of variables listed in Equations (3.58)–(3.59). The other boundary conditions are

$$\bar{T}^{(1)}_{R_r} = 0 = \bar{T}^{(2)}_{R_r}, \quad \text{at } r = 0, \tag{3.65}$$

$$\frac{k_R}{k_C}\bar{T}^{(1)}_{R_r} = \bar{T}_{C_r}, \qquad \bar{T}^{(1)}_R = \bar{T}_C, \tag{3.66}$$

$$\frac{k_R}{k_{SC}}\bar{T}^{(2)}_{R_r} = \bar{T}^{(2)}_{SC_r}, \bar{T}^{(2)}_R = \bar{T}^{(2)}_{SC} \quad \text{at } r = R_r, \tag{3.67}$$

$$\bar{T}_{C_r} = 0 = \bar{T}_{SC_r}, \quad \text{at } r = 1. \tag{3.68}$$

Also, by integrating Equations (3.60)–(3.63) with respect to r over their appropriate r-domains and using (3.64)–(3.68), we find that

$$\int_0^{R_r} \bar{T}^{(1)}_R \cdot r \, \mathrm{d}r = \int_0^{R_r} \bar{T}^{(2)}_R \cdot r \, \mathrm{d}r = 0, \tag{3.69}$$

$$\int_{R_r}^1 \bar{T}_C \cdot r \, \mathrm{d}r = \int_{R_r}^1 \bar{T}^{(2)}_{SC} \cdot r \, \mathrm{d}r = 0.$$

These expressions will be used in the final search for H_0 and G_0 as defined in (3.2). The remaining boundary conditions are those defined at the interface $\xi = \varepsilon H(r)$, in Equations (3.34)–(3.36). Using Equation (3.2) and Taylor series expansions, we define the following boundary conditions at this interface

$$-H_0 B'_{R_0}(l_C) = B_{R_2}(l_C) - \frac{r^2}{4}(B''_{R_0}(l_C) - \mathrm{Pe}_R\, B'_{R_0}(l_C)) + \bar{T}^{(1)}_R(r, 0), \tag{3.70}$$

$$-H_0 B'_{R_0}(l_C) = B_{R_2}(l_C) - \frac{r^2}{4}(B''_{R_0}(l_C) - \mathrm{Pe}_R\, B'_{R_0}(l_C)) + \bar{T}^{(2)}_R(r,0), \tag{3.71}$$

$$\begin{aligned} -H_0 B'_{C_0}(l_C) \;=\; & B_{C_2}(l_C) + \log(r)\overline{\beta_C}(\Theta(l_C) - B_{C_0}) \\ & + \left(\frac{\log(r)}{2} - \frac{r^2}{4}\right)(B''_{C_0}(l_C) - \mathrm{Pe}_C\, B'_{C_0}(l_C)) + \bar{T}_C(r,0), \end{aligned} \tag{3.72}$$

$$\begin{aligned} -H_0 B'_{SC_0}(l_C) \;=\; & B_{SC_2}(l_C) + \log(r)\overline{\beta_{SC}}(\Theta(l_C) - B_{SC_0}) \\ & + \left(\frac{\log(r)}{2} - \frac{r^2}{4}\right)(B''_{SC_0}(l_C) - \mathrm{Pe}_{SC}\, B'_{SC_0}(l_C)) + \bar{T}^{(2)}_{SC}(r,0), \end{aligned} \tag{3.73}$$

$$K_C \bar{T}^{(2)}_{SC_\xi} - \bar{T}_{C_\xi} = 0. \tag{3.74}$$

In the above, $B_{R_2}(l_C)$, $B_{C_2}(l_C)$, and, $B_{SC_2}(l_C)$ are unknown quantities. We determine these by multiplying the Equations (3.70)–(3.73) by r and integrating over the appropriate r-domain. The resulting expressions for $B_{R_2}(l_C)$, $B_{C_2}(l_C)$, and, $B_{SC_2}(l_C)$ are substituted back in (3.70)–(3.73). After simplifying, we find that

$$-H_0 B'_{R_0}(l_C) = \left(\frac{R_r^2}{8} - \frac{r^2}{4}\right)[B''_{R_0}(l_C) - \mathrm{Pe}_R\, B'_{R_0}(l_C)] + \bar{T}^{(1)}_R(r,0), \tag{3.75}$$

$$-H_0 B'_{R_0}(l_C) = \left(\frac{R_r^2}{8} - \frac{r^2}{4}\right)[B''_{R_0}(l_C) - \mathrm{Pe}_R\, B'_{R_0}(l_C)] + \bar{T}^{(2)}_R(r,0), \tag{3.76}$$

$$-H_0 B'_{C_0}(l_C) = \overline{\beta_C}\left[\frac{1}{2} + \frac{R_r^2\,\log(R_r)}{(1-R_r^2)} + \log(r)\right](\Theta(l_C) - B_{C_0}(l_C)) \tag{3.77}$$

$$+\left[\frac{3 + 4(R_r^2\,\log(R_r) - \log(r)) - 2(R_r^2 + r^2)}{8(1-R_r^2)}\right]\cdot(B''_{C_0}(l_C) - \mathrm{Pe}_C\, B'_{C_0}(l_C)) + \bar{T}_C(r,0),$$

$$-H_0 B'_{SC_0}(l_C) = \overline{\beta_{SC}}\left[\frac{1}{2} + \frac{R_r^2\,\log(R_r)}{(1-R_r^2)} + \log(r)\right](\Theta(l_C) - B_{SC_0}(l_C)) \tag{3.78}$$

$$+\left[\frac{3 + 4(R_r^2\,\log(R_r) - \log(r)) - 2(R_r^2 + r^2)}{8(1-R_r^2)}\right]\cdot(B''_{SC_0}(l_C) - \mathrm{Pe}_{SC}\, B'_{SC_0}(l_C)) + \bar{T}_{SC}(r,0).$$

We can derive similar equations for G_0. The details can be found in [60]. To complete the analysis for $O(\varepsilon^2)$, we solve (3.60)–(3.63) using separation of variables.

After applying the boundary conditions, we find the solutions can be expressed as

$$\bar{T}^{(1)}_R(r,\xi) = \sum a_n\, \mathrm{e}^{\lambda_n \xi} J_0(\lambda_n r), \tag{3.79}$$

$$\bar{T}_C(r,\xi) = \sum b_n\, \mathrm{e}^{\lambda_n \xi}\left[Y_0(\lambda_n r) - \frac{Y_1(\lambda_n)}{J_1(\lambda_n)} J_0(\lambda_n r)\right], \tag{3.80}$$

$$\bar{T}_R^{(2)}(r,\xi) = \sum c_n \, \mathrm{e}^{-\lambda_n \xi} J_0(\lambda_n r), \tag{3.81}$$

$$\bar{T}_{SC}^{(2)}(r,\xi) = \sum d_n \, \mathrm{e}^{-\lambda_n \xi} \left[Y_0(\lambda_n r) - \frac{Y_1(\lambda_n)}{J_1(\lambda_n)} J_0(\lambda_n r) \right], \tag{3.82}$$

where J_0, J_1, Y_0, and Y_1 are Bessel functions and the λ_n are the zeros of the Bessel function J_1. At $\xi = 0$, we have the condition that, $\bar{T}_R^{(1)}(r,0) = \bar{T}_R^{(2)}(r,0)$, so it follows that $a_n = c_n$. Also, from the latent heat condition (3.74), we find that $b_n = -K_C d_n$.

If we now multiply Equation (3.77) by $B'_{SC_0}(l_C)$ and (3.78) by $B'_{C_0}(l_C)$, equate them, and use (3.80), we may solve for $\bar{T}_{SC}^{(2)}(r,0)$. Substituting this in Equation (3.78), we find the following expression for H_0:

$$\begin{aligned} H_0 \;=\; & \left[\frac{\overline{\beta_C}(T_{C_M} - \Theta(l_C)) + K_C \overline{\beta_{SC}}(T_{C_M} - \Theta(l_C))}{K_C B'_{SC_0}(l_C) + B'_{C_0}(l_C)} \right] \times \left[\frac{1}{2} + \frac{R_r^2 \log(R_r)}{(1 - R_r^2)} + \log(r) \right] \\ & - \left[\frac{B''_{C_0}(l_C) - \mathrm{Pe}_C \, B'_{C_0}(l_C) + K_C (B''_{SC_0}(l_C) - \mathrm{Pe}_{SC} \, B'_{SC_0}(l_C))}{K_C B'_{SC_0}(l_c) + B'_{C_0}(l_C)} \right] \\ & \times \left[\frac{3 + 4(R_r^2 \log(R_r) - \log(r)) - 2(R_r^2 + R^2)}{8(1 - R_r^2)} \right]. \end{aligned} \tag{3.83}$$

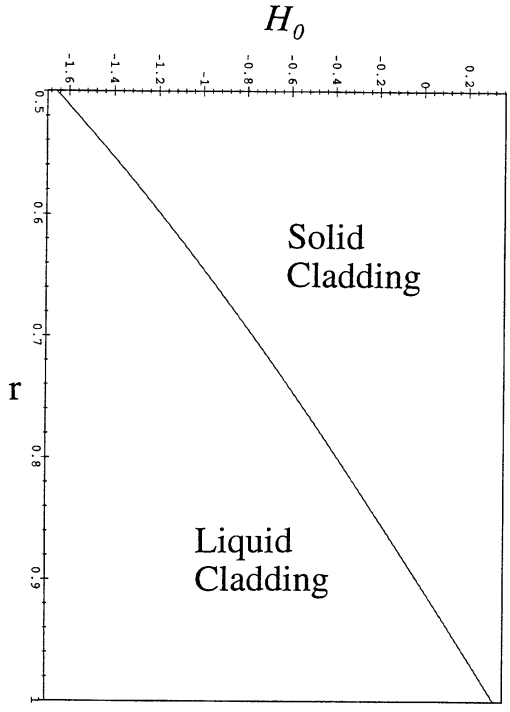

Figure 6. Shape of the clad liquid–solid interface.

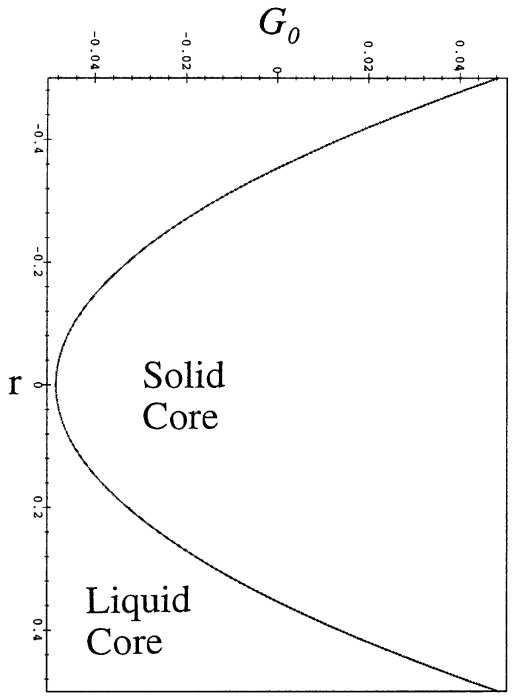

Figure 7. Shape of the core liquid–solid interface.

The numerators in Equation (3.83) represent radial heat transfer near the solidification front l_C, while the denominators correspond to axial heat transfer near this front. The denominator

is negative in this case, so that the concavity of the curved isotherm is set by the direction of heat transfer determined by the temperature difference $T_{C_M} - \Theta(l_C)$ in the expression for H_0. For the data listed in Table 1, Equation (3.83) is plotted in Figure 6. This figure corresponds to the lower portion of the clad region shown in Figure 2. Here the exit temperature of the mold is 513 K, which is greater than the melting point of tin, which is 505·06 K. Thus, the clad material closer to the mold is hotter than the melting point, so that heat transfers in radially. The material close to the core is cooler by comparison, due to axial heat transfer. This accounts for the shape definition in Figure 6, with faster solidification near the core. If we were to include the flow details near l_C, the expression for H_0 would have an additional term corresponding to the zero-mass flow, $\tilde{V}_C$. Young and Chait [39] provide an example of such an analysis for the float-zone configuration.

Similar to the analaysis for H_0, we find that

$$G_0 = \left(\frac{R_r^2}{8} - \frac{r^2}{4}\right) \times \left[\frac{B''_{R_0}(l_R) - \mathrm{Pe}_R\, B'_{R_0}(l_R) + K_R(B''_{SR_0}(l_R) - \mathrm{Pe}_{SR}\, B'_{SR_0}(l_R))}{K_R B'_{SR_0}(l_R) + B'_{R_0}(l_R)}\right]. \quad (3.84)$$

This function is plotted in Figure 7. Notice that G_0 is parabolic in shape, although the magnitude of the deflection is an order of magnitude smaller than in the clad zone, as in Figure 6. Near $z = l_R$, the heat being transferred in from the clad region heats the core above the melting point, so near the cladding, the core material is warmer. The middle of the core is cooler by comparison, so it solidifies quicker. Similar to the discussion for H_0, the numerator characterizes radial heat transfer, while the denominator represents axial heat transfer. Thus, achieving a planar interface requires operating conditions which minimize radial heat transfer at the front and/or which maximize the sum of axial temperature gradients between the core liquid and solid phases at this location.

As a limiting case, consider Equations (3.11), (3.17), (3.19–3.22). When the core and clad thermal conductivities and melting points are equal, the system does not distinguish between core and clad material. The first two terms of the differential equations in (3.19) and (3.21), evaluated at $z = l_R$, are identical to the expressions in the numerator of (3.84). Hence, we can replace these expressions by the third and fourth terms in (3.19) amd (3.21) as $R_r \to 1$. The result is the numerator expression, $\overline{\beta_C}(T_{C_M} - \Theta(l_C)) + K_C\overline{\beta_{SC}}(T_{C_M} - \Theta(l_C))$, in (3.83). Hence, Equations (3.83) and (3.84) collapse to the same equation and we have a single material system with parabolic isotherms and solidification front, which agrees with the numerical simulations for thin rods [2, 5].

Table 2. Constant velocity, $V = 18$ mm/min, clad thickness, $\hat{R}_r = 2{\cdot}5$ mm and mold cooler distance, $\hat{L} = 20$ mm

T K	l_C	l_R
515	0·4109	1·127
530	0·7464	1·283
540	0·8673	1·346
550	0·9532	1·405

Table 3. Constant initial temperature, $T = 575$ K, clad thickness, $\hat{R}_r = 2{\cdot}5$ mm, and mold cooler distance, $\hat{L} = 20$ mm.

V mm/min	l_C	l_R
6	0·5201	1·038
12	0·6762	1·173
18	0·8088	1·316
24	0·9319	1·472

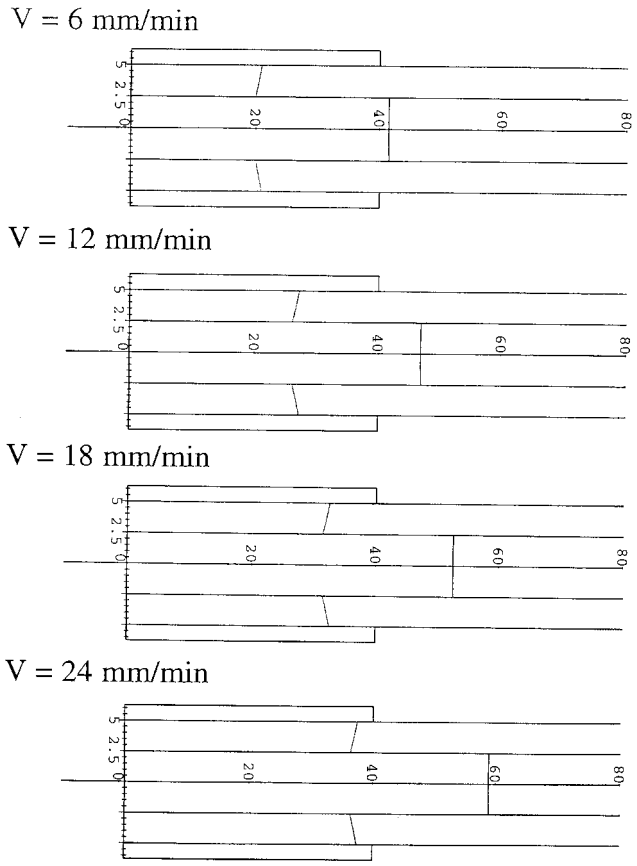

Figure 8. Interface shapes (in mm) taken from the nondimensional data in Table 3.

4. Parametric study

We now examine the system's response to a change in the various casting variables. As stated earlier, the materials considered here are pure tin as a cladding, and a Sn-Pb alloy for the core [4]. The input data used in the simulations can be found in Table 1 [2, 4, 61, 62].

First, let the casting speed V remain constant. If we raise the input temperature of the melt, the position of the fronts should move closer to the mold exit, since it will take longer to reach the melting point. Likewise, lowering the initial temperature will result in the front moving farther back into the mold. The results in Table 2 are consistent with this explanation.

Next, we let the initial temperature remain fixed. An increase in the casting velocity should move the front closer to the mold exit. This happens because the material is moving faster compared to the axial heat transfer. Likewise, a decrease in the casting speed will result in the front solidifying further into the mold. These results are reported in Table 3. Figure 8 shows the shapes (in dimensional units) of the solidification fronts. Equations (2.1), (2.2), (3.2), (3.83) and (3.84), and the results in Table 3, were used to define the fronts. We note that the temperature isotherms are more parabolic in the mold region and flatter near the water spray. This is consistent with numerical simulations of Ohno Casting of a single material [2, 5] and reflects that radial heat transfer is largest in the mold region. Additionally, because of

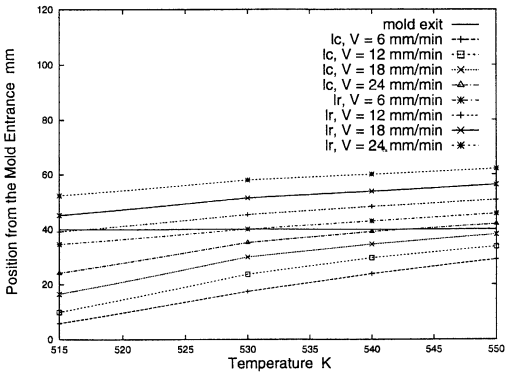

Figure 9. Locations of the mean clad and core solidification fronts for the fixed values $\hat{R}_r = 2{\cdot}5$ mm and $\hat{L} = 60$ mm.

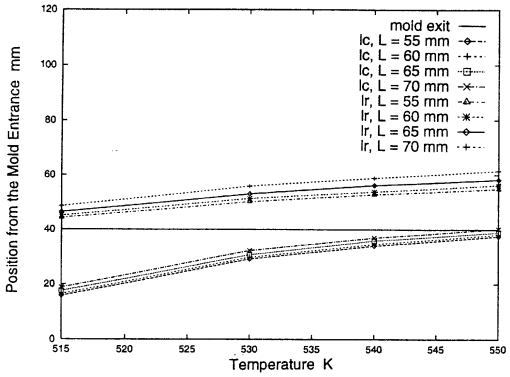

Figure 10. Locations of the mean clad and core solidification fronts for the fixed values $\hat{R}_r = 2{\cdot}5$ mm and $V = 18$ mm/min.

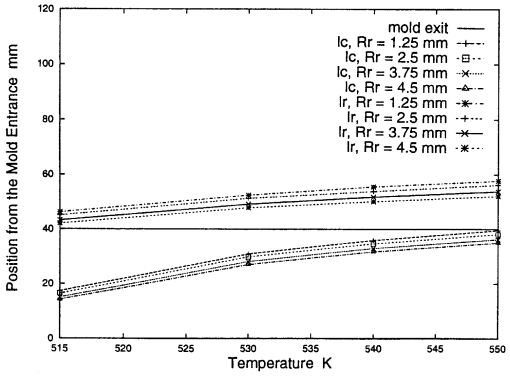

Figure 11. Locations of the mean clad and core solidification fronts for the fixed values $V = 18$ mm/min and $\hat{L} = 60$ mm.

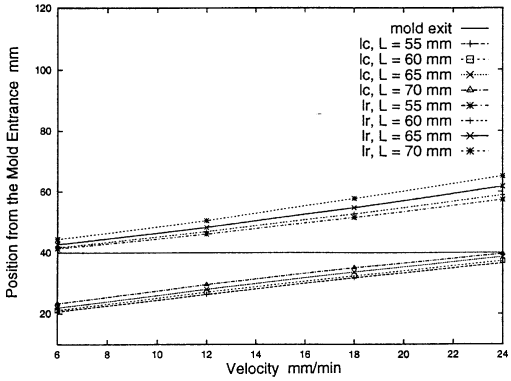

Figure 12. Locations of the mean clad and core solidification fronts for the fixed values $T = 535$ K and $\hat{R}_r = 2{\cdot}5$ mm.

its smaller thermal diffusivity, the cladding acts as an insulating layer to the core, reducing the radial heat transfer, as discussed above. The practical implication is that the flat core solidification front should lead to reduced radial segregation when casting multi-component alloys. Further, since the core front appears to remain flat over a wide range of processing conditions, practioners can focus on setting the operating conditions to keep the clad front near the mold exit.

Table 4. Constant velocity, $V = 18$ mm/min, clad thickness, $\hat{R}_r = 2{\cdot}5$ mm, and initial temperature, $T = 575$ K.

$\hat{L}$ mm	l_C	l_R
55	0·7971	1·291
60	0·8088	1·316
65	0·8400	1·367
70	0·8712	1·441

Table 5. Constant velocity, $V = 18$ mm/min, initial temperature, $T = 575$ K, and mold cooler distance, $\hat{L} = 20$ mm.

$\hat{R}_r$ mm	l_C	l_R
4·5	0·7113	1·094
3·75	0·7698	1·267
2·5	0·8088	1·316
1·25	0·8361	1·350

Next, we fix the velocity and initial melt temperature and vary the location of the water spray. By moving the water spray closer to the mold exit, we expect the positions of the fronts

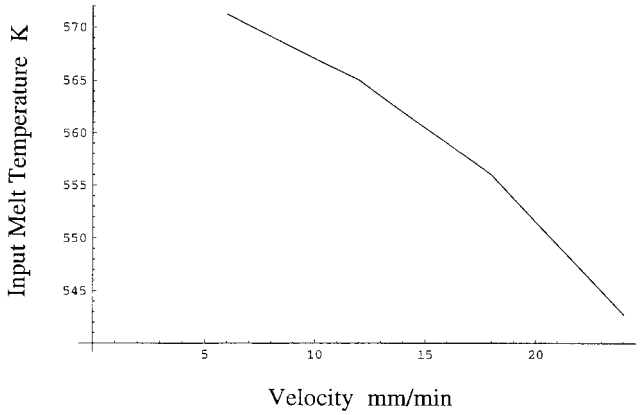

Figure 13. Operating points to set the location of $\hat{l}_C$ at the mold exit (40 mm) for the fixed values $\hat{R}_r = 2{\cdot}5$ mm and $\hat{L} = 60$ mm.

to be farther into the mold. This happens due to an increase in the axial heat transfer. In a similar fashion, moving the water spray further from the mold exit results in the interface position moving out toward the end of the mold. The results are listed in Table 4.

Finally, keeping the previous quantities constant, we vary the thickness of the cladding. For all the earlier examples, $\hat{R}_r = 2{\cdot}5$ mm. Notice that the thinner the clad layer, *i.e.*, the higher value of $\hat{R}_r$, the further into the mold the front solidifies. Since the core has a higher thermal diffusivity, the axial heat transfer is enhanced. The results are listed in Table 5.

Consider the location of the clad and core solidification fronts shown in Figure 9. For sufficiently large input melt temperature and casting velocity, the position of the clad interface $\hat{l}_C$ moves outside the mold (> 40 mm), This is not necessarily desirable. Once outside the mold, the clad growth occurs in a float zone configuration [8, 10]. This is not accounted for in this model. On the other hand, if the interface is too far into the mold, the friction caused by the solid clad material scraping against the surface of the mold will cause tearing of the clad material. This occurs for slower casting velocities and lower input melt temperatures.

In Figure 10, we see that the position of the water spray also affects the front location, though not as drastically as do changes in the casting velocity.

In Figure 11, we see that the solidification fronts are sensitive to the clad thickness, due to the mismatch in thermal diffusivity between the cladding and core. Finally, Figure 12 indicates that the system is much more sensitive to changes in the input melt temperature and casting velocity than to changes in the water spray location. Furthermore, the front locations appear to vary linearly with changes in the casting speed.

The above results are summarized in Figure 13. Using the data from Figure 9, we plot the input melt temperature and casting velocity which set the location of the clad front $\hat{l}_C$ at the mold exit. For operating points above the curve, $\hat{l}_C$ will be outside the mold. If we move the water spray closer to the mold exit, *i.e.* decrease $\hat{L}$, the operating curve will be slightly above that shown in Figure 13. Hence, there is a slightly larger operating domain for which $\hat{l}_C$ remains inside the mold.

There are a number of extensions that can be made to this work. Ignoring the mandrel will definitely change the system heat transfer, and should be examined thoroughly to improve the accuracy of the model. Also, the effects of fluid dynamics, such as the input liquid pressure, contribute to the cast quality [1, 6]. Furthermore, the composition of binary systems can

influence the cast quality [6]. Finally, dissolution between the solid cladding and the liquid core is an important phenomenon to be considered [4].

Acknowledgement

This work was supported by NSF Grant DMS 95-32021.

References

1. H. Soda, F. Chabchoub, W. H. Lam, S. A. Argyroopoulos and A. McLean, The horizontal Ohno continuous casting process: Process variables and their effects on casting stability. *Cast Metals* 4 (1991) 12–19.
2. F. Chabchoub, J. Mostaghimi and S. A. Argyroopoulos, A three dimensional mathematical model for the horizontal Ohno continuous casting process. *Transp. Phenom. Materials* 169 (1992) 69–74.
3. H. Soda, F. Chabchoub, S. A. Argyroopoulos and A. McLean, Experimental study of the horizontal Ohno continuous casting system. *Can. Metallurg. Quart.* 31 (1992) 231–239.
4. H. Soda, A. Ichinose, G. Motoyasu, A. Ohno and A. McLean, A new fabrication method for the casting of cored materials. *Cast Metals* 5 (1992) 95–102.
5. F. Chabchoub, S. A. Argyroopoulos and J. Mostaghimi, Mathematical modeling and experimental measurements on the horizontal Ohno continuous casting process for pure tin. *Can. Metallurg. Quart.* 33 (1994) 73–88.
6. H. Soda, G. Motoyasu, A. McLean and A. Ohno, Effects of process variables on cast surface quality of alloy rod produced by the Ohno continuous casting (OCC) process. *Can. Metallurg. Quart.* 33 (1994) 89–98.
7. H. Soda, A. McLean, G. Motoyasu and A. Ohno, Ohno continuous casting. *Adv. Mater. Proc.* April (1995) 43–45.
8. H. Soda, A. McLean, Z. Wang and G. Motoyasu, Pilot-scale casting of single-crystal copper wires by the Ohno Continuous Casting process. *J. Mat. Sci.* 30 (1995) 5438–5448.
9. H. Soda, C. K. Jen, G. Motoyasu, S. Okumura, A. Ohno and A. McLean, Fabrication and characterization of aluminum clad aluminum-copper alloy cored rod. *Mat. Sci. Tech.* 11 (1995) 1174–1179.
10. H. Soda, G. Motoyasu, A. McLean, C.K. Jen and O. Lisboa, Method for continuous casting of metal wire and tube containing optical fibre. *Mat. Sci. Tech.* 11 (1995) 1169–1173.
11. V. Alexiades and A. D. Solomon, *Mathematical Modeling of Melting and Freezing Processes (1st Edn.)* Bristol: Hemisphere (1993) 323 pp.
12. A. A. Samarskii, P. N. Vabishchevich, O. P. Iliev and A. G. Churbanov, Numerical simulation of convection/diffusion phase change problems-a review. *Int. J. Heat Mass Transfer* 36 (1993) 4095–4106.
13. S. Weinbaum and L. M. Jiji, Singular perturbation theory for melting or freezing in finite domains initially not at the fusion temperature. *J. Appl. Mech.* 44 (1977) 25–30.
14. M. M. Yan and P. N. S. Huang, Perturbation solutions to phase change problem subject to convection and radiation. *J. Heat Trans.* 101 (1979) 96–100.
15. G. W. Barry and J. S. Goodling, A Stefan problem with contact resistance. *J. Heat Transfer* 109 (1987) 820–825.
16. Z. Dursunkaya and S. Nair, A moving boundary problem in a finite domain. *J. Appl. Mech.* 57 (1990) 50–56.
17. D. S. Cohen and T. Erneux, Changing time history in moving boundary problems, *SIAM J. Appl. Math.* 50 (1990) 483–489.
18. D. E. Glass, M. N. Ozisik and S. S. McRae, Formulation and solution of hyperbolic Stefan problem. *J. Appl. Phys.* 70 (1991) 1190–1197.
19. C. Charach and I. Rubinstein, Pressure-temperature effects in planar Stefan problems with density change. *J. Appl. Phys.* 71 (1992) 1128–1137.
20. H. T. Chen and J. Y. Lin, Hybrid Laplace transform technique for Stefan problems with radiation-convection boundary condition. *Int. J. Heat Mass Transfer* 35 (1992) 3345–3351.
21. C. K. Hsieh and C. Y. Choi, Solution of one- and two-phase melting and solidification problems imposed with constant or time-variant temperature and flux boundary conditions. *J. Heat Trans.* 114 (1992) 524–528.
22. J. Y. Hsieh and C. C. Hwang, Nonlinear morphological instabilities in directional solidification – An integral approximation. *J. Appl. Phys.* 76 (1994) 2765–2772.

23. P. Tritscher and P. Broadbridge, A similarity solution of a multiphase Stefan problem incorporating general non-linear heat conduction. *Int. J. Heat Mass Transfer* 37 (1994) 2113–2121.
24. M. Conti, Planar solidification of a finite slab: effects of the pressure dependence of the freezing point. *Int. J. Heat Transfer* 38 (1995) 65–70.
25. C. K. Hsieh, Exact solutions of Stefan problems for a heat front moving at constant velocity in a quasi-steady state. *Int. J. Heat Mass Transfer* 38 (1995) 71–79.
26. R. H. Rangel and X. Bian, The inviscid stagnation-flow solidification problem. *Int. J. Heat Mass Transfer* 39 (1996) 1591–1602.
27. T. J. Fitzgerald and R. F. Singer, An analytical model for optimal directional solidification using liquid metal cooling. *Met. Mat. Trans. A, Phys. Met Mat. Sci.* 28A (1997) 1377–1383.
28. D. A. Tarzia and C. V. Turner, The one-phase supercooled Stefan problem with a convective boundary condition. *Q. Appl. Math.* 55 (1997) 41–50.
29. X. Bian and R. H. Rangel, Stagnation-flow solidification on a finite thickness substrate. *Int. J. Heat Mass Transfer* 41 (1998) 244–247.
30. I. Rubinstein and B. Zaltzman, Morphological instability of similarity solution to the Stefan problem with undercooling and surface tension. *Q. Appl. Math.* 56 (1998) 341–354.
31. L. H Ungar, M. J. Bennet and R. A. Brown, Cellular interface morphologies in directional solidification. III. The effects of heat transfer and solid diffusivity. *Phys. Rev. B* 31 (1985) 5923–5930.
32. L. H. Ungar and R. A. Brown, Cellular interface morphologies in directional solidification. IV. The formation of deep cells. *Phys. Rev. B* 31 (1985) 5931–5940.
33. K. Brattkus and S. H. Davis, Directional solidification with heat losses. *J. Cryst. Growth*. 91 (1988) 538–556.
34. R. A. Brown and D. H. Kim, Modelling of directional solidification: from Scheil to detailed numerical simulation. *J. Cryst. Growth.* 109 (1991) 50–65.
35. K. Tsiveriotis and R. A. Brown, Nonlinear local dynamics of the melt crystal interface of a binary alloy in directional solidification. *Phys. rev. B-Condensed Matter* 48 (1993) 13495–13501.
36. K. Tsiveriotis and R. A. Brown, Long-time scale dynamics observed in directional solidification of a binary alloy. *Phys. Rev. B-Condensed Matter* 49 (1994) 12724–12737.
37. K. Brattkus, Directional solidification into static stability. *J. Fluid Mech.* 304 (1995) 143–159.
38. G. W. Young and A. J. Chait, Steady State Thermal-Solutal Diffusion in a Float Zone. *J. Cryst. Growth* 96 (1989) 65–95.
39. G. W. Young and A. Chait, Surface tension driven heat, mass, and momentum transport in a two-dimensional float zone. *J. Cryst. Growth* 106 (1990) 445–466.
40. G. W. Young and J. A. Heminger, Modeling the time-dependent growth of single crystal fibers. *J. Cryst. Growth* 178 (1997) 410–421.
41. *ASM Handbook Volume 15 Casting*. United States: ASM International (1992) 937 pp.
42. J. Campbell, *Castings*. Oxford: Butterworth–Heinemann Ltd (1991) 288 pp.
43. J. Szekely, J. W. Evans and J. K. Brimacombe, *The Mathematical and Physical Modeling of Primary Metals Processing Operations*. New York: John Wiley & Sons, Inc. (1988) 261 pp.
44. E. Takeuchi and J. K. Brimacombe, The formation of oscillation marks in the continuous casting of steel slabs. *Metallurg. Trans. B* 15B (1984) 493–509.
45. G. J. Kor, An analysis of the fluid flow of liquid mold powder in the space between the continuous casting mold and the steel shell. *Proceedings: 2nd Processing Technical Conference 2* (1981) 124–132.
46. R. Bommaraju and E. Saad, Mathematical modelling of lubrication capacity of mold fluxes. *Steelmaking Conf. Proc.* (1990) 281–296.
47. I. B. Risteski, A mathematical model of the conduct of the molten powder in the gap between the mold and the slab in the vicinity of the meniscus. *Steel and Metals Mag.* 28 (1990) 661–665.
48. E. Anzai, T. Ando, T. Shigezumi, M. Ikeda and T. Nakano, Hydrodynamic behavior of molten powder in meniscus zone of continuous casting Mold. *Nippon Steel tech. Rep.* 34 (1987) 31–40.
49. J. K. Brimacombe, Design of continuous casting machines based on a heat flow analysis: State of the art review. *Can. Metallurg. Quart.* 15 (1976) 163–175.
50. A. A. Sfeir and J. A. Clumpner, Continuous casting of cylindrical ingots. *J. Heat Trans* (1977) 29–34.
51. I. V. Samarasekera and J. K. Brimacombe, Application of mathematical models for the improvement of billet quality. *Steelmaking Conf. Proc.* (1991) 91–103.
52. D. Mazumdar, A consideration about the concept of effective thermal conductivity in continuous casting. *ISIJ* (1989) 524–528.

53. D. Mazumdar and R. Verma, A predictive mathematical model for analysis of continuous casting of steel. *Trans. Indian Inst. Metals* 42 (1989) 447–459.
54. A. Moitra and B. G. Thomas, Application of a thermo-mechanical finite element model of steel shell behavior in the continuous slab casting mold. *76th Steelmaking Conference, Dallas, TX, Iron and Steel Society, Warrendale, PA 76* (1993) 657–667.
55. P. J. Flint, A three-dimensional finite difference model of heat transfer, fluid flow, and solidification in the continuous slab caster. *Steelmaking Conf. Proc.* (1990) 481–490.
56. B. G. Thomas, Mathematical modelling of the continuous slab casting mold: A state of the art review. *Steelmaking Conf. Proc.* (1991) 105–118.
57. J. DiLellio and G. W. Young, An asymptotic model of the mold region in a continuous steel caster. *Metallurg. Trans.* (1995) 1225–1241.
58. H. K. Kuiken, The cooling of low-heat-resistance cylinders by radiation. *J. Engng. Math.* 13 (1979) 97–106.
59. H. K. Kuiken and P. J. Roksnoer, Analysis of the temperature distribution in FZ silicon crystals. *J. Cryst. Growth* 47 (1979) 29–42.
60. S. A. Morman, An asymptotic approach to mathematically modeling the Ohno continuous casting process. Masters Thesis, The University of Akron. May (1997).
61. *Metals Handbook. Properties and selection: Nonferrous alloys and special-purpose materials*. United States: ASM International 2(ed. 10) (1990) 1328 pp.
62. *Metals Handbook. Properties and selection: Nonferrous alloys and special-purpose materials*. United States: ASM International 2(ed. 9) (1979) 855 pp.